Robotic Metamorphosis by Origami Exoskeletons

Shuhei Miyashita,[1,2]* Steven Guitron,[1] Shuguang Li,[1] and Daniela Rus[1]*

[1]Computer Science and Artificial Intelligence Laboratory, Massachusetts Institute of Technology, 32 Vassar Street, Cambridge, MA, 02139, USA.

[2]Department of Electronic Engineering, University of York, Heslington, York, YO10 5DD, UK.

*Correspondence to: shuhei.miyashita@york.ac.uk, rus@csail.mit.edu

Abstract: Changing the inherent physical capabilities of robots by metamorphosis has been a long-standing goal of engineers. However, this task is challenging because of physical constraints in the robot body, each component of which has a defined functionality. Inspired by nature, roboticists have designed self-reconfiguring robots, which are cellular machines consisting of a set of identical unit-modules that can change their body geometry independently to match the structure to the task (*1– 11*), or adapt their hardware and software in real time (*12–14*). Self-reconfiguring systems, however, have limitations in their on-site extensibility, because of the large scale of today's unit modules and the complex administration of their coordination, which relies heavily on on-board electronic components. In this study, we present a novel approach to extending and changing the capabilities of a robot by enabling metamorphosis using self-folding origami "exoskeletons". We show how a cubical magnet "robot" can be remotely moved using a controllable magnetic field to hierarchically develop different morphologies by interfacing with different origami exoskeletons. Activated by heat, each exoskeleton is self-folded from a rectangular sheet, extending the capabilities of the initial robot, such as enabling the manipulation of objects or locomotion on the ground, water, or air. Activated by water, the exoskeletons can be removed and are interchangeable. Thus, the system represents an end-to-end (re)cycle. Here, we present several robot and exoskeleton designs, devices, and experiments with robot metamorphosis using exoskeletons.

One Sentence Summary: This study shows a novel process of robotic morpho-functional extension using interchangeable self-folding origami sheets.

Introduction

Some life forms have inherent metamorphic capabilities and acquire different functionalities in their developmental stages. Butterflies and beetles morph from larva and acquire the ability to fly (*15*). Hermit crabs switch their housings on demand, obtain materials from the environment, and change parts of their body. In comparison, most current hard-bodied machines, such as today's industrial robots, have a fixed architecture and cannot develop on-the-fly new functionalities. Robots that aim for a flexible architecture have thus been designed to deliver multiple locomotion modalities through several means: (I) by equipping them with redundant components (*16–19*), (II) by constructing structures or tools on-site (*20, 21*), (III) by designing modular systems capable of self-reconfiguration (*22–24*), or (IV) by creating origami-inspired bodies with programmable configurations (*5–7, 9, 25–30*). Each of these approaches can achieve a wide

range of malleable capabilities (*31*,*32*), but in practice, extending the inherent physical capabilities of robots is challenging because of the electro-mechanical limitations of the robot body and the lack of (re)productivity of physical elements. Using metamorphosis in nature as an inspiration, we introduce an alternative approach to extending the capabilities of a robot by enabling it to cyclically acquire multiple self-folding origami sheets called "exoskeletons." Like an egg, the system commences with a cubic magnet "robot," called *Primer*. This robot hierarchically develops its morphology by combining with different exoskeletons; for example, it moves faster, becomes bigger, or uses different locomotion processes on the ground, in the water, and in the air. An example of metamorphosis is shown in Fig. 1, where *Primer* develops morphology through the processes of equipping exoskeletons; as a result, it obtains the ability to walk and roll. Removing an exoskeleton, analogous to insect molting, can be done by directing the robot into water, which dissolves the holding arms of the exoskeleton.

Our prior work contributes knowledge on static origami structures achievable from a single sheet (5) and mobile origami systems where the body has a fixed origami structure and a fixed function (7, 29). In the present study, we contribute to the concepts of robot metamorphosis using exoskeletons, specific designs and devices capable of metamorphosis, and end-to-end experiments, and demonstrate how one shared origami structure acts as an "engine" capable of adding and removing different exoskeletons to achieve different body shapes and functions. The convergence of materials and machines enables this approach to be robotic metamorphosis by combining a compact design for function, efficient reconfiguration, and a large space for achievable, fine resolution body shapes. The proposed approach demonstrates the advantages of origami-inspired manufacturing, namely, versatility, (re-)usability, and accessibility of components (*33*), which provide simplicity and structural redundancy to the mechanism.

Results

We demonstrate robotic metamorphosis with a suite of acquisitions and removals of robot exoskeletons. Each exoskeleton is designed to generate a different robot morphology that supports different capabilities. The system consists of *Primer*, an environment with a controllable magnetic field that enables the movement of the robot, two heating pads (Peltier element) for assembling the exoskeletons, a water reservoir for removing the exoskeleton, and a ramp for assisting gliding. The representative sequences for this system are shown in Fig. 2 (a–f) and (g-h), with a scaling up of the body size and gliding performance, respectively. The ability to walk is useful when the maintenance of posture is necessary, for example, when carrying a load, pushing an object, or acting as a patch *in vivo* (*32*), where a small step size is needed. Acquiring large body sizes provides various advantages, such as the ability to walk faster, transport a large object, or maintain stability against turbulence. A typical exoskeleton acquisition takes approximately 3 min to complete, and a typical molting process completes in less than a minute with the assistance of body vibration.

The transformations of the robot are shown as a state diagram in Fig. 3; origami self-folding robots can cyclically acquire modalities for walking (*Walk-bot*), scaling by a large homothetic exoskeleton (*Scaled walk-bot*), rolling by cylindrical morphology (*Wheel-bot*), sailing on water by boat morphology (*Boat-bot*), and gliding in the air by wing morphology (*Glider-bot*). The scaling exoskeleton *Scaled walk-bot* allows *Walk-bot* to move faster and shovel objects. The wheel exoskeleton gives *Walk-bot* two flat circular structures on both sides of the body, which

act as wheels. It can roll on a plane 2.3 times faster than *Walk-bot*. The boat exoskeleton provides *Walk-bot* floating capability on water with enhanced buoyancy for a load carriage 1.86 times its own weight. *Boat-bot* features high side walls and a swept shape to maximize volumetric capacity underwater while minimizing drag. The glider exoskeleton endows *Walk-bot* with the capability to reach a distant place by gliding. As a dandelion distributes seeds blown by the wind, or maple trees release propeller-shaped seeds that flutter down to reach a distance, the ability to glide would be useful when deploying robots or switching environments. Our experiments successfully demonstrate each end-to-end cycle that starts with *Primer*, extends *Primer* with one of the four exoskeletons, performs the capabilities enabled by the exoskeleton, and removes the exoskeleton.

The comparison of the locomotion speeds of *Walk-bot* and *Scaled walk-bot* at different magnetic field frequencies is shown in Fig. 4. With the periodic application of a magnetic field at angles of 27°, 63°, 90°, and -63° in the dorsal plane, both robots move on the stage in the direction of the magnetic field. Their walking speed reaches a maximum of 3.07 cm/s when a magnetic flux density 0.35 mT is applied at 9 Hz (0.34 cm/step). We applied a magnetic field five times stronger on *Scaled walk-bot* than that on *Walk-bot* for pivoting, with the difference in the moment of inertia considered by reflecting the squares of distance between the pivot point and the center of the magnet. When a constant frequency oscillatory magnetic flux density 1.75 mT is applied at 6 Hz, *Scaled walk-bot* walks at a maximum speed of 4.66 cm/s (0.78 cm/step), which is 51.9% faster than the fastest speed of *Walk-bot*, supported by the 128% increase in step size. *Walk-bot* can walk faster with the *Scaled walk-bot* exoskeleton. *Scaled walk-bot* enables a larger step size. The larger step size allows us to use lower frequencies to achieve the same speed. The bigger step size is also useful for shoveling and moving a mass, and for travelling over terrain with gaps. The other enhanced capabilities of the robot were quantitatively analyzed with respect to locomotion speed, floating capability, and gliding capability. For the details of each exoskeleton, see Supplementary Materials.

Discussion

Robots with fixed architectures will perform the task for which they are designed well, but will perform poorly on different tasks in different environments. This study introduces the possibility of developing a robot that can extend and switch its capabilities by putting on exoskeletons and changing its body shape. We explored how the use of materials and a task-centered design can empower robots with a wide range of capabilities, with the complexity of the fixed robot body traded off with the design and control challenges of changing shape. The robot could acquire these capabilities to perform additional tasks, such as driving through water and burrowing or anchoring in sand. Exoskeletons could also form fixtures or simple tools, such as a drill, water scoop, shovel, cutter, or a grabber. They can likewise be potentially used for bio-mimicry functions, such as tail cutting or camouflaging. The principle of on-site morphing with custom exoskeletons to rapidly create new types of robots has the potential to provide more flexibility to robotic operations at difficult-to-access sites in multiple fields, such as in-space manufacturing, incision-free medical procedures (*32*), deep sea construction, and disaster site rescue operations. Although the devices demonstrated in this study are small in scale, robots with similar metamorphosis capabilities can be created using the same principles at a wide variety of scales.

Suppose a robot needs to execute task A, which requires, for example, traversing water,

followed by task B, which requires, for example, shoveling an area. Instead of creating a robot whose body can execute tasks A and B simultaneously, we propose designing a simpler robot, *Primer*, that can act as the engine for a multitude of tasks. Each task has a corresponding exoskeleton designed to wrap around and connect to *Primer*. *Primer* can pick up the exoskeleton by using a self-folding process activated by heat, and remove it by using a self-disassembly process activated by water. For our example tasks A and B, *Primer* acts as the engine that can travel to pick up the exoskeleton for task A (sailing), execute the sailing task, drive to discard the exoskeleton for sailing upon completion of this task, drive to pick up the exoskeleton for task B (shoveling), and continue. The key insight in this work is that through the use of novel materials that can be self-folded and self-disassembled, we simplify the design of robot systems, while increasing the range of tasks that they can perform. The key technical contributions of our study include (1) developing the design of *Primer* and exoskeletons for scaling the robot to move with larger steps, shoveling, rolling, sailing, and gliding; (2) creating the methods for acquiring and removing exoskeletons; and (3) conducting end-to-end experiments for robot metamorphosis and task execution for each capability.

The capabilities of robots are defined by what their bodies can do and how their "brains" can control these bodies to execute tasks. The body, the brain, and the tasks that can be executed have a tight coupling. We believe that this work will open the door to the development of a new class of robots that are compact and can be specialized and customized to execute a wide range of tasks. This study is the first demonstration of on-site, on-demand robotic morpho-functional acquisition and disposal achieved purely on a material basis, in which the same material unit can be used to flexibly add and remove a part of the structure and reshape its operative boundary.

Materials and Methods

The Platform and Experimental Condition

Fig. 5 shows the newly designed platform, which provides an environment for testing the robot. It consists of: a stage; two Peltier elements for robot self-assembly; a water reservoir for robot disassembly and sailing experiments; a ramp on which *Glider-bot* slides for gliding; with a motor-assisted leaning pad (Servo motor HS-55, *HiTec*) positioned adjacent to the ramp to initiate the slide; four solenoid coils (diameter: 21 cm) inclined 45° from the horizontal plane, directed toward the center of the stage from beneath, and the supporting electronics for current control. The stage is 30 cm in diameter with an actuatable workspace of 25 cm. The water reservoir is an arc-shaped lane sloping down toward the middle part. A robot can enter and exit the reservoir from either side, or it can directly jump in from the middle part where no protection wall exists. The deepest part is 1.52 cm in depth, and the average slope angle is 10°. The ramp has a traveling length of 47 cm for *Glider-bot*, and it is set at an inclination angle of 33° from the horizontal plane. *Glider-bot* is released at a height of 112 cm from the ground. The currents for producing magnetic fields are controlled with a microcontroller (Arduino Esplora) and four motor drivers (SyRen25, *Dimension Engineering*) through serial communication.

The remote actuation of the robot is possible by transferring magnetic force and torque to *Primer* with the electromagnetic coils (*34*–*43*). The platform used in the experiments for this work provides a significantly wider range of controllable space; most of the other coil systems were developed to cover merely several centimeters of workspace. The attachment mechanisms of the exoskeletons require precise localization, which can be provided via magnetic sensing,

vision, or an external tracking and localization system. While autonomous localization using magnetic sensing was demonstrated in our platform in (*44*), in this work we focus on the metamorphosis of robots and reduce experimental complexity by relying on a human operator to remotely control the alignment between the robot and its exoskeletons, and the direction of the robot's movement. The patterns of the applied magnetic fields are adjusted to each locomotion modality to reflect the dynamics and body mass. See Supporting Materials for details.

Using the control mechanism, we conducted five end-to-end experiments for each design. We started with *Primer*, created *Walk-bot* (1st-shape), created 2nd-shape extended from *Walk-bot*, demonstrated the new capabilities, and transformed the robot from the 2nd-shape to the 1st-shape. We also conducted multiple experiments for the respective transitions and consistently achieved success. During these experiments, the biggest challenge was the accurate alignment control of *Walk-bot* to the exoskeleton sheet, which is required to transition from one shape to another.

Self-folding

The self-folding of exoskeletons is achieved using the tensile stress of a pre-stretched thermo-shrinking polymer film (Polyvinyl Chloride, deformation occurs at 65°C, 0.03 mm thickness, *Shrink Bag*), laminated on both sides with two rigid sheets (Mylar sheets, 0.05 mm thickness, *Mylar*) by using silicone adhesive (High-Temperature Glue-on-a-Roll, *McMaster-Carr*). By differentiating the crease widths on the front and back sides of the self-folding sheet pattern, the folding direction can be controlled (*45*). When the sheet is exposed to heat at the glass transition temperature or marginally higher, a difference in shear stress is induced in the contractive layer between the two opposite faces, where the side with a wider gap contracts more and in turn creates a fold (*45*). All the creases are designed to fold simultaneously, but they experience speed differences, depending on the loads placed on the creases and the distance from the Peltier element. The fabrication of self-folding sheets is completed using a computer-aided cutting process with either a laser cutter or vinyl cutter, and manual lamination processes. The Peltier elements (Therma TEC 926-1279-ND, *LairdTech*) used are 43.9 × 39.9 cm^2 in size and can differentiate up to 63°C between both faces. The temperature rise is triggered manually with a constant current (2.2 A) to the respective elements in an open-loop manner.

Docking and "Molting" mechanism

A holding arm/latch assembly equipped in the exoskeleton sheet enables *Walk-bot* to interface with the exoskeleton. The assembly consists of four latches: two front latches are longer to wrap around *Primer* of *Walk-bot*, whereas two back latches hold the tail of *Walk-bot* tightly to allow the torque to be transmitted through the structure (Fig. 6). The two front arms have wide, connected segments so that during the self-folding process, they can stay rigid enough to completely encase the magnet. The two back arms have thin, disconnected segments so that they can fold over the low tail. The roots of the arms were made of water-soluble paper, ASWT-1 (*Aquasol*). When exposed to water, the water-soluble tape dissolves; it separates the arms from the exoskeleton and enables *Walk-bot* to be released. In our investigation, dissolving a latch from the body by physically vibrating the exoskeleton at 2 Hz took 18 s (five samples), on average. In the experiments, 5 min was allotted to allow all latch connections to completely dissolve.

References

1. K. Kotay, D. Rus, M. Vona, C. McGray, The self-reconfiguring robotic molecule, in *Proceedings of the IEEE/RSJ International Conference on Intelligent Robots and Systems (IROS)* (IEEE, 1998), pp. 424–431.
2. S. Murata, H. Kurokawa, Self-reconfigurable robots. *IEEE Robotics & Automation Magazine.* **14**, 71–78 (2007).
3. K. Gilpin, A. Knaian, D. Rus, Robot pebbles: One centimeter module for programmable matter through self-disassembly, in *Proceedings of the IEEE International Conference on Robotics and Automation (ICRA)* (IEEE, 2010), pp. 2485–2492.
4. M. Yim, W-M. Shen, B. Salemi, D. Rus, M. Moll, H. Lipson, E. Klavins, G. S. Chrikjian, Modular self-reconfigurable robot systems. *IEEE Robotics & Automation Magazine.* **14**, 43–50 (2007).
5. E. Hawkes, B. An, N. M. Benbernou, H. Tanaka, S. Kim, E. D. Demaine, D. Rus, R. J. Wood, Programmable matter by folding. *Proc. Natl. Acad. of Sci. U.S.A.* **107**, 12441–12445 (2010).
6. C. D. Onal, M. T. Tolley, R. J. Wood, D. Rus, Origami-inspired printed robots. *IEEE/ASME Transactions on Mechatronics***. 20**, 2214–2221 (2014).
7. S. Felton, M. T. Tolley, E. Demaine, D. Rus, R. J. Wood, A method for building self-folding machines. *Science.* **345**, 644–646 (2014).
8. A. Firouzeh, J. Paik, Robogami: A fully integrated low-profile robotic origami. *Journal of Mechanisms and Robotics.* **7**, 021009 (2015).
9. K. C. Cheung, E. D. Demaine, J. R. Bachrach, S. Griffith, Programmable assembly with universally foldable strings (moteins). *IEEE Transactions on Robotics.* **27**, 718 (2011).
10. A. Cully, J. Clune, D. Tarapore, J.-B. Mouret, Robots that can adapt like animals. *Nature.* **521**, 503–507 (2015).
11. M. Boyvat, J.-S. Koh, R. J. Wood, Addressable wireless actuation for multijoint folding robots and devices. *Science Robotics.* **2**, eaan1544 (2017).
12. H. Lipson, J. B. Pollack, Automatic design and manufacture of artificial lifeforms. *Nature.* **406**, 974–978 (2000).
13. V. Zykov, E. Mutilinaios, B. Adams, H. Lipson, Self-reproducing machines. *Nature.* **435**, 163–164 (2005).
14. J. Bongard, Morphological change in machines accelerates the evolution of robust behavior. *Proc. National Academy of Sciences* **108**, 1234–1239 (2011).
15. N. A. Campbell, J. B. Reece, L. Urry, M. L. Cain, S. A. Wasserman, P. V. Minorsky, R. B. Jackson, *Biology: A Global Approach* (Pearson, 2014).
16. J. D. Dickson, J. E. Clark, Design of a multimodal climbing and gliding robotic platform. *IEEE/ASME Transactions on Mechatronics.* **18**, 494–505 (2013).
17. M. A. Woodward, M. Sitti, MultiMo-Bat: A biologically inspired integrated jumping-gliding robot. *International Journal of Robotics Research.* **33**, 1511–1529 (2014).

18. A. Vidyasagar, J.-C. Zufferey, D. Floreano, M. Kovac, Performance analysis of jump-gliding locomotion for miniature robotics. *Bioinspiration & Biomimetics.* **10**, 025006 (2015).

19. K. Jayaram, R. J. Full, Cockroaches traverse crevices, crawl rapidly in confined space, and inspire a soft, legged robot. *Proc. National Academy of Sciences* **113**, E950–E957 (2016).

20. S. Revzen, M. Bhoite, A. Macasieb, M. Yim, Structure synthesis on-the-fly in a modular robot, in *Proceedings of the IEEE/RSJ International Conference on Intelligent Robots and Systems (IROS)* (2011), pp. 4797–4802.

21. L. Wang, L. Brodbeck, F. Iida, Mechanics and energetics in tool manufacture and use: A synthetic approach. *Journal of the Royal Society Interface.* **11**, DOI: 10.1098/rsif.2014.0827 (2014).

22. J. Hiller, H. Lipson, Automatic design and manufacture of soft robots. *IEEE Transactions on Robotics.* **28**, 457–466 (2012).

23. E. Klavins, Programmable self-assembly. *IEEE Control System Magazine.* **27**, 43–56 (2007).

24. J. W. Romanishin, K. Gilpin, D. Rus, M-blocks: Momentum-driven, magnetic modular robots, in *Proceedings of the IEEE/RSJ International Conference on Intelligent Robots and Systems (IROS)* (2013), pp. 4288–4295.

25. I. Shimoyama, H. Miura, K. Suzuki, Y. Ezura, Insect-like microrobots with external skeletons. *IEEE Control Systems.* **13**, 37–41 (1993).

26. A. M. Hoover, E. Steltz, R. S. Fearing, RoACH: An autonomous 2.4g crawling hexapod robot, in *Proceedings of the IEEE/RSJ International Conference on Intelligent Robots and Systems (IROS)* (2008), pp. 26–33.

27. J. P. Whitney, P. S. Sreetharan, K. Ma, R. J. Wood, Pop-up book MEMS. *Journal of Micromechanics and Microengineering.* **21**, 115021 (2011).

28. M. Noh, S.-W. Kim, S. An, J.-S. Koh, K.-J. Cho, Flea-inspired catapult mechanism for miniature jumping robots, *IEEE Transactions on Robotics.* **28**, 1007 (2012).

29. S. Miyashita, S. Guitron, M. Ludersdorfer, C. Sung, D. Rus, An untethered miniature origami robot that self-folds, walks, swims, and degrades, in *Proceedings of the IEEE International Conference on Robotics and Automation (ICRA)* (2015), pp. 1490–1496.

30. J. Morgan, S. P. Magleby, L. L. Howell, An approach to designing origami-adapted aerospace mechanisms, *Journal of Mechanical Design.* **138**, 052301 (2016).

31. K. Kuribayashi, K. Tsuchiya, Z. You, D. Tomus, M. Umemoto, T. Ito, M. Sasaki, Self-deployable origami stent grafts as a biomedical application of Ni-rich TiNi shape memory alloy foil. *Materials Science and Engineering A.* **419**, 131–137 (2006).

32. S. Miyashita, S. Guitron, K. Yoshida, S. Li, D. D. Damian, D. Rus, Ingestible, controllable, and degradable origami robot for patching stomach wounds, in *Proceedings of the IEEE International Conference on Robotics and Automation (ICRA)* (2016), pp. 909–916.

33. R. J. Lang, *Origami Design Secrets* (CRC Press, Taylor & Francis Group, 2012).

34. T. Honda, K. I. Arai, K. Ishiyama, Micro swimming mechanisms propelled by external magnetic fields. *IEEE Transactions on Magnetics.* **32**, 5085 (1996).

35. K. Ishiyama, M. Sendoh, K. Arai, Magnetic micromachines for medical applications. *Journal of Magnetism and Magnetic Materials.* **242**, 41–46 (2002).

36. S. Martel, J-B. Mathieu, O. Felfoul, A. Chanu, E. Aboussouan, S. Tamaz, P. Pouponneau, Automatic navigation of an untethered device in the artery of a living animal using a conventional clinical magnetic resonance imaging system. *Applied Physics Letters.* **90**, 114105 (2007).

37. K. Vollmers, D. R. Frutiger, B. E. Kratochvil, B. J. Nelson, Wireless resonant magnetic microactuator for untethered mobile microrobots. *Applied Physics Letters.* **92**, 144103 (2008).

38. S. Floyd, C. Pawashe, M. Sitti, Modeling and experimental characterization of an untethered magnetic micro-robot. *International Journal of Robotics Research.* **28**, 1077– 1094 (2009).

39. M. P. Kummer, J. J. Abbott, B. E. Kratochvil, R. Borer, A. Sengul, B. J. Nelson, OctoMag: An electromagnetic system for 5-DOF wireless micromanipulation, in *Proceedings of the IEEE International Conference on Robotics and Automation (ICRA)* (2010), pp. 1006–1017.

40. S. Miyashita, E. Diller, M. Sitti, Two-dimensional magnetic micro-module reconfigurations based on inter-modular interactions. *International Journal of Robotics Research.* **32**, 591–615 (2013).

41. E. Diller, J. Giltinan, G. Z. Lum, Z. Ye, M. Sitti, Six-degree-of-freedom magnetic actuation for wireless microrobotics. *International Journal of Robotics Research.* **35**, 114–128 (2015).

42. B. E. Kratochvil, D. R. Frutiger, K. Vollmers, B. J. Nelson, Visual servoing and characterization of resonant magnetic actuators for decoupled locomotion of multiple untethered mobile microrobots, in *Proceedings of the IEEE International Conference on Robotics and Automation (ICRA)* (2009), pp. 1010–1015.

43. E. Diller, J. Giltinan, M. Sitti, Independent control of multiple magnetic microrobots in three dimensions. *International Journal of Robotics Research.* **32**, 614–631 (2013).

44. S. Guitron, A. Guha, S. Li, D. Rus, Autonomous locomotion of a miniature, untethered origami robot using hall effect sensor-based magnetic localization, in *Proceedings of the IEEE International Conference on Robotics and Automation (ICRA)* (2017), pp. 4807–4813.

45. S. Miyashita, C. D. Onal, D. Rus, Self-pop-up cylindrical structure by global heating, in *Proceedings of the IEEE/RSJ International Conference on Intelligent Robots and Systems (IROS)* (2013), pp. 4065–4071.

46. C. Sung, R. Lin, S. Miyashita, S. Yim, S. Kim, D. Rus, Self-folded soft robotic structures with controllable joints, in *Proceedings of the IEEE International Conference on Robotics and Automation (ICRA)* (2017), pp. 580–587.

Acknowledgments: Funding: Supported by NSF grants 1240383 and 1138967. Author contributions: S.M. and S.L. conceived the concept; S.M., S.L., and D.R. designed the research; S.M., S.G., and S.L. developed the system; S.G and S.L. performed the experiments; S.G. analyzed the data; and S.M., S.G., and D.R. wrote the paper. D.R. provided funding.

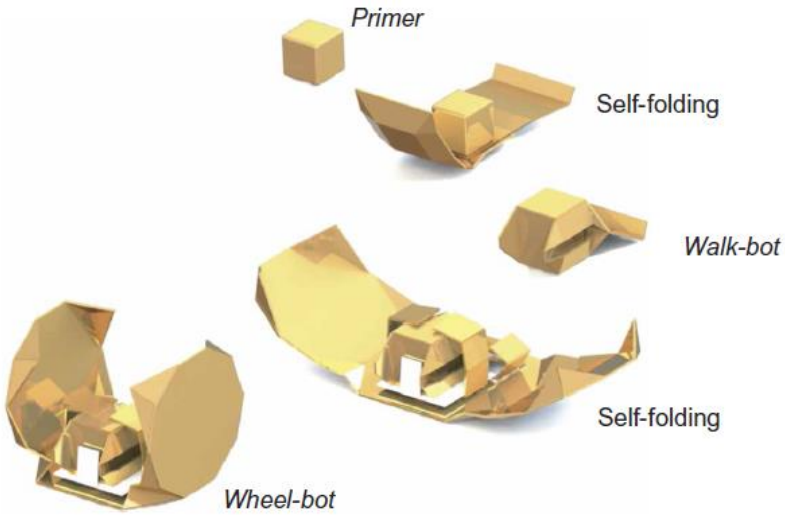

Fig. 1. Example of robotic metamorphosis by origami exoskeletons. *Primer* metamorphoses into *Walk-bot* and then to *Wheel-bot*, hierarchically equipping and obtaining different locomotion capabilities.

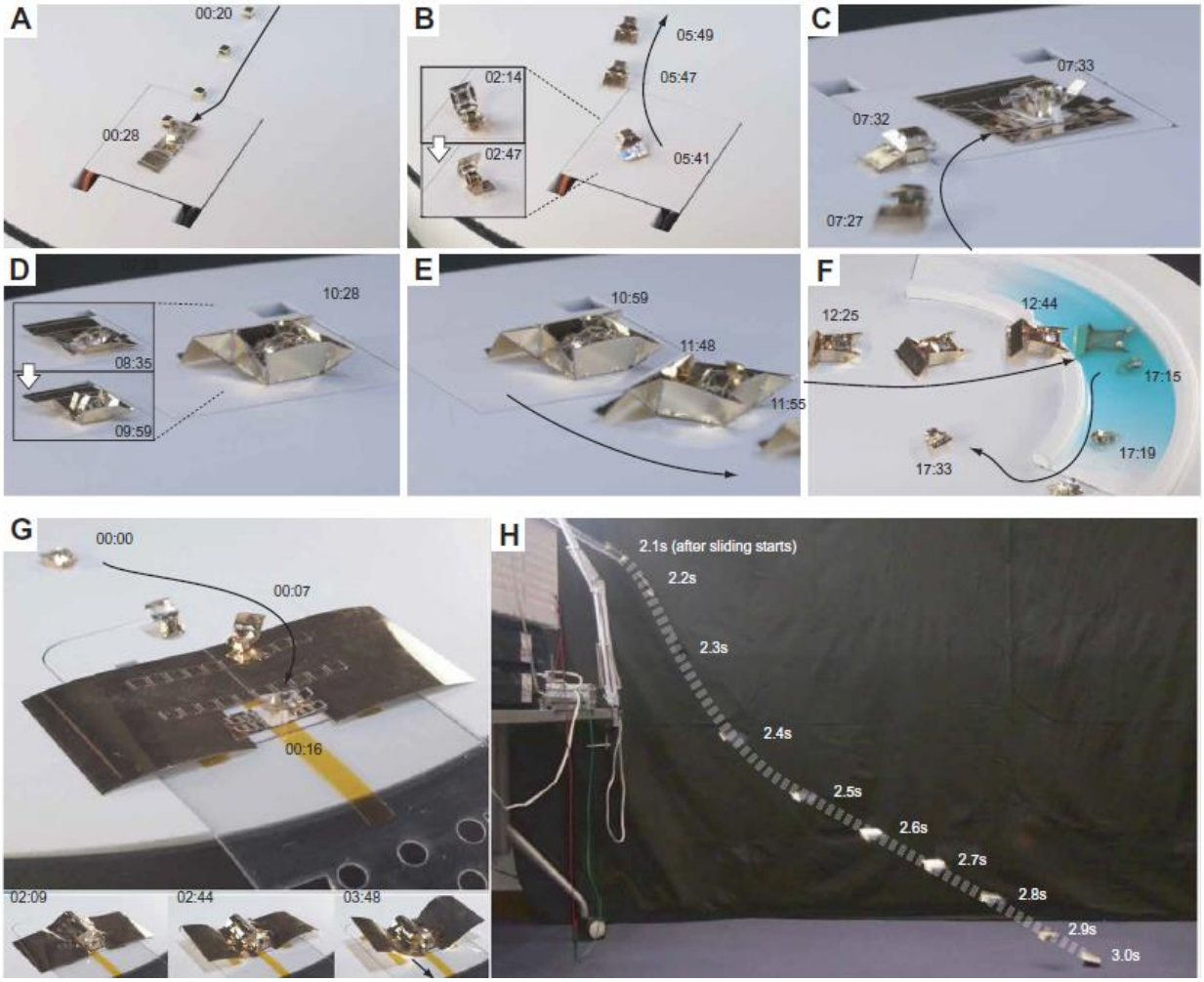

Fig. 2. Entire demonstrations of *Scaled walk-bot* (a-f) and *Glider-bot* (g,h). (a) *Primer* rolls remotely guided by a rotating magnetic field and can coalesce with *Walk-bot* self-folding sheet, the exoskeleton that encases and holds it. (b) *Primer*, which now features a minimal form for walking, supported by a tail for pitch stabilization, is forthwith capable of locomotion because of the eccentric body mass distribution (termed *Walk-bot*, the self-folding process in the small windows). (c-d) *Walk-bot* can further walk to another exoskeleton. The second exoskeleton can be equipped in the same way; it is held by self-folding arms that contain dissolving parts. After *Walk-bot* aligns on top of the latch module, the pit, four arms self-fold and hold *Walk-bot* such that *Primer* can transmit magnetic torque through the contact surface of the exoskeletons. At this point, the system morphs into a second shape, which has a larger but analogical morphology to *Walk-bot* (termed *Scaled walk-bot*). (f) For "taking off" the second exoskeleton, *Scaled walk-bot* enters a water reservoir where the four holding arms dissolve, and the released *Walk-bot* from the second exoskeleton can climb out of the reservoir and leave the exoskeleton discarded in the water. (g,h) Transformation of *Walk-bot* to *Glider-bot*, and the gliding performance. *Walk-bot* acquires a wing and, assisted by a ramp, can reach 26 times its body length (129 cm) from the stage by gliding through the air from a height of 112 cm. See Movies 1 and 4 in Supplementary Materials for the entire experiments.

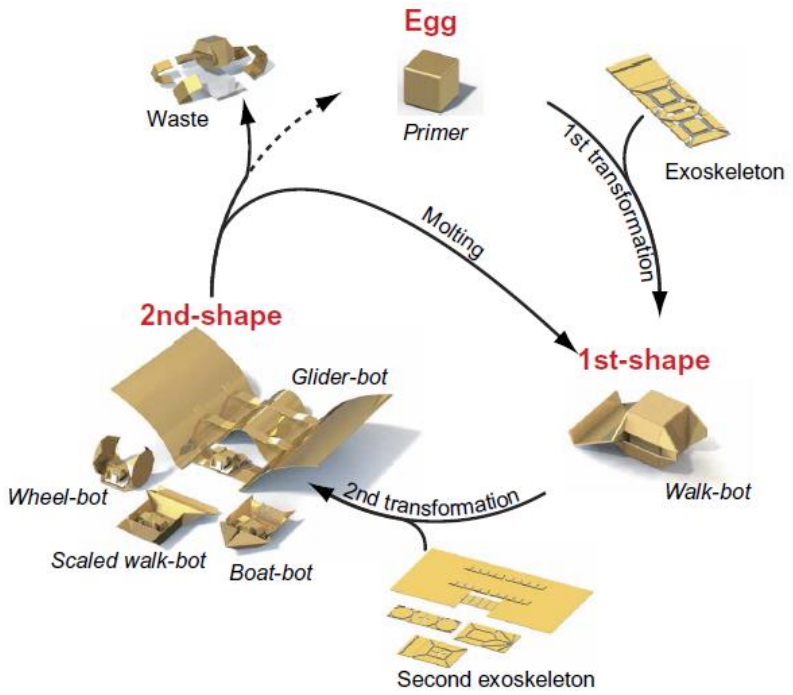

Fig. 3. Robotic metamorphic cycle. Starting as *Primer* at the top, the system morphs into the first shape, *Walk-bot*, as shown on the right. *Walk-bot* can subsequently transform into the second shape by integrating a self-folding exoskeleton. We demonstrate four new capabilities, namely, scaling up (*Scaled walk-bot*), sailing (*Boat-bot*), rolling (*Wheel-bot*), and gliding (*Glider-bot*), which can only be achieved by equipping exoskeletons, but other capabilities are also possible. The second shape can recover the morphologies of earlier stages by removing ("molting") the exoskeleton. The disassembly process of the second exoskeleton transforming to *Walk-bot* can be performed by dissolving the holding arms in water. The disassembly process of *Walk-bot*, which is beyond the scope of this study, can be performed by making the body of *Walk-bot* dissolvable to a specific solvent. We demonstrated this process with polyester-made origami robots that could dissolve relevant body parts after submersion in the solvent (*29*).

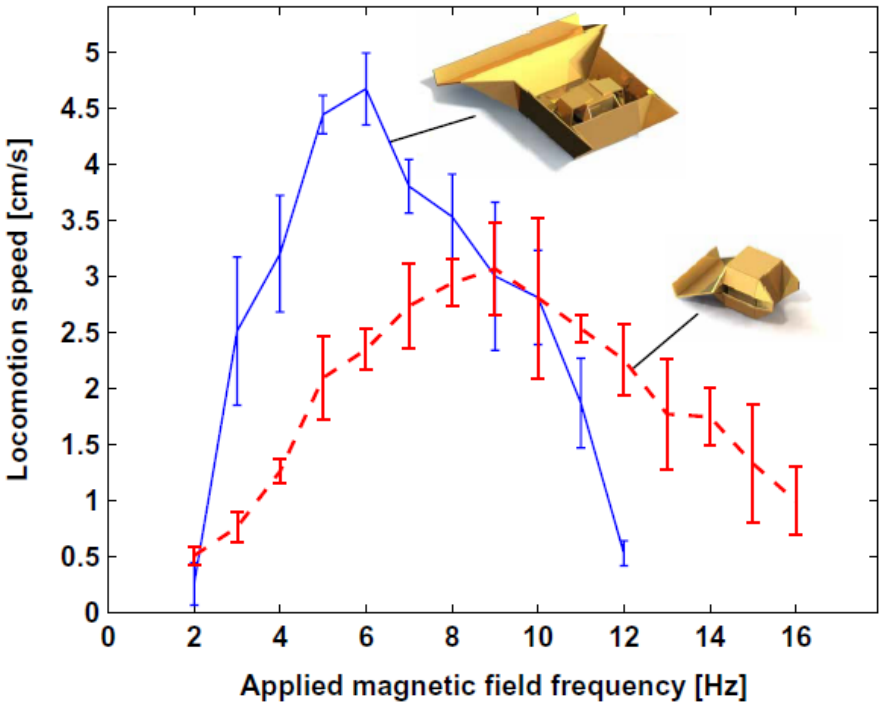

Fig. 4. Comparison of locomotion speeds between *Walk-bot* and *Scaled walk-bot*. With the scaled morphology, an increase in walking speed of more than 50% was observed.

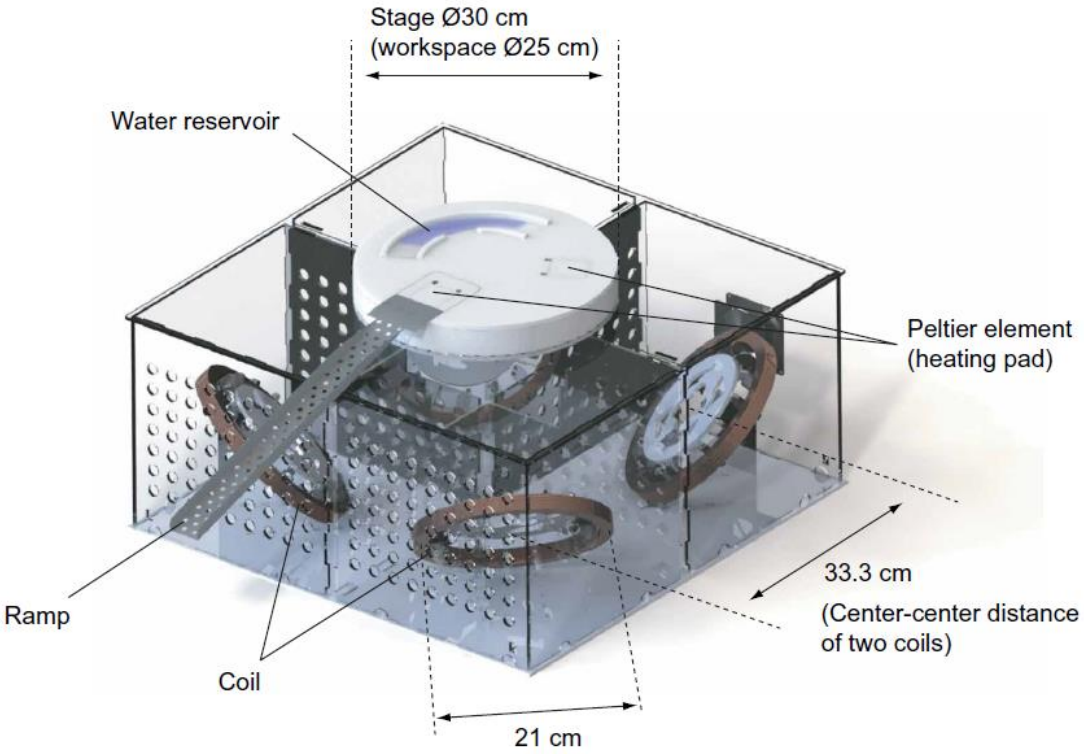

Fig. 5. The platform, which consists of four solenoid coils, two Peltier elements, a water reservoir, and a ramp.

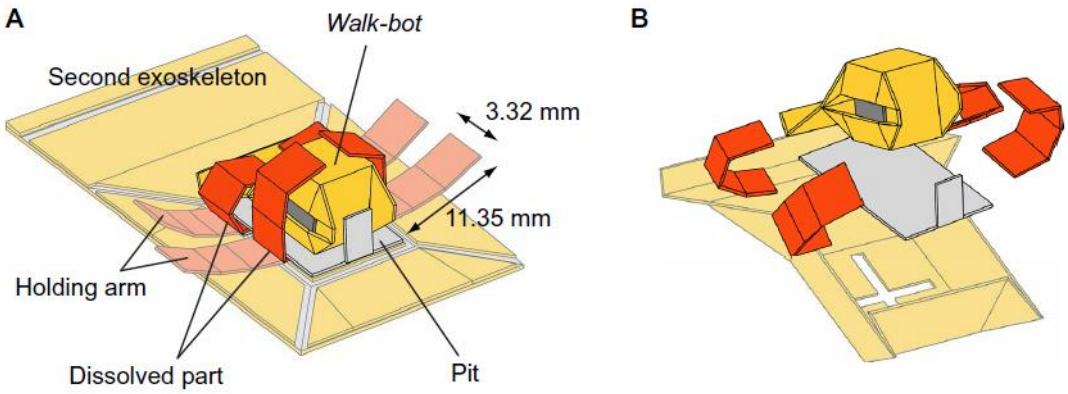

Fig. 6. Docking and molting mechanism. (a) Four arms, whose roots are made of water-dissolvable material, tightly hold *Walk-bot*. (b) Upon immersion in water, the roots dissolve and release *Walk-bot*.

Supplementary Materials
Remote Magnetic Control
Primer Control
Walk-bot
Scaled walk-bot
Wheel-bot
Boat-bot
Glider-bot
Multimedia Extension

Table 1 – 4
Fig S1 – S9
Movie 1 – 4

Supplementary Materials for Robotic Metamorphosis by Origami Exoskeletons

Shuhei Miyashita, Steven Guitron, Shuguang Li, Daniela Rus

corresponding author: shuhei.miyashita@york.ac.uk, rus@csail.mit.edu

In Supplementary Materials, we describe Magnetic control, design, control, and performance of *Primer*, *Walk-bot*, *Scaled walk-bot*, *Wheel-bot*, *Boat-bot*, and *Glider-bot* at length.

Remote Magnetic Control

The following sections derive the control of the coils by currents to obtain targeted magnetic torque and force for controlling the robot. The four coils (numbered $i \in 1, ..., 4$) are placed in counter-clockwise order seen from above at regular intervals around the central vertical axis in the lower hemisphere of diameter $d\,(= 65.2\,\mathrm{cm})$ of the stage. This configuration provides the upper half hemisphere with an open space for robot operation. Each coil is inclined 45° from the horizontal plane such that the axes of symmetry intersect at the center of the sphere (set as the origin, ${}^{G}O$, of global coordinate ${}^{G}\hat{X}\hat{Y}\hat{Z}$, where the ${}^{G}\hat{X}$-$\hat{Y}$ plane is set horizontal, see Fig. S1).

The local coordinate frame of coil i, ${}^{i}\hat{x}\hat{y}\hat{z}$ is defined for each coil, where the origins of the local coordinate frames are located at the centroids of the coils ${}^{i}o$. The ${}^{i}\hat{x}$-$\hat{y}$ plane is parallel to the diametrical plane of the coil, and ${}^{i}\hat{z}$ is normal to the plane, coinciding with other ${}^{j}\hat{z}$ ($j \in 1, ..., 4; j \neq i$) axes of the coils at ${}^{G}O$.

The magnetic flux density produced by coil i along the central axis at position z relative to

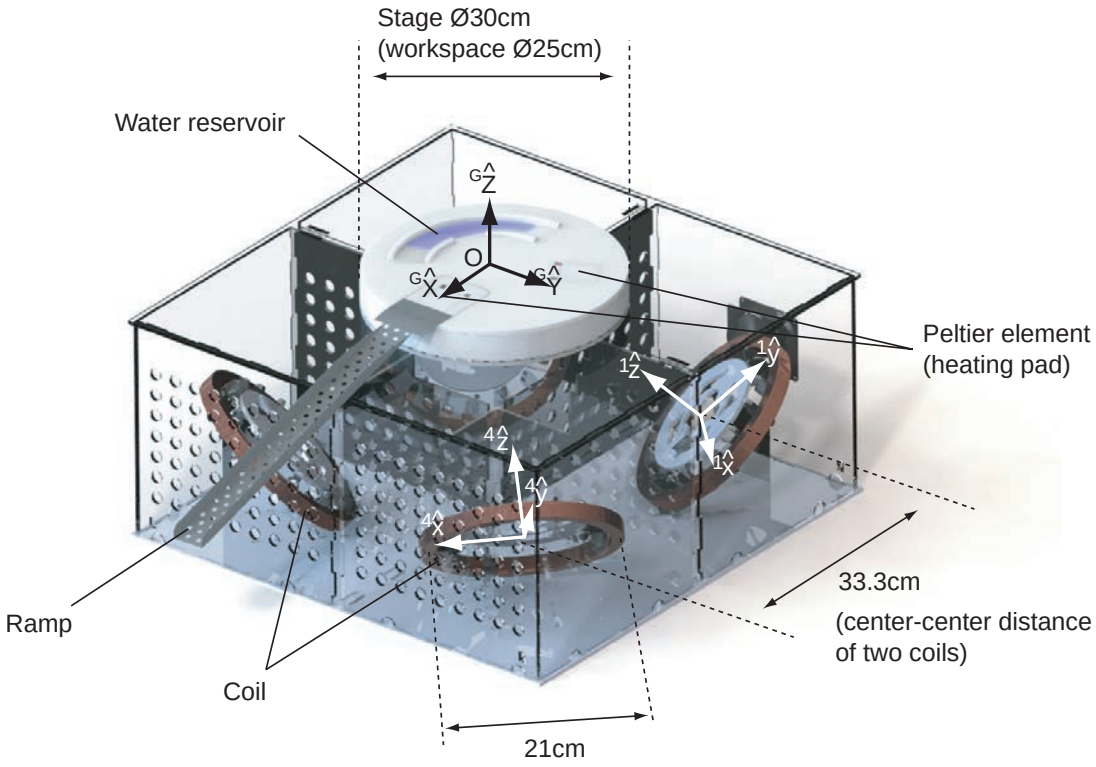

Figure S1: The platform. Coordinates are added from Fig. 5.

a coordinate frame ${}^i\hat{x}\hat{y}\hat{z}$ is

$$ {}^i\vec{b}_i = \begin{pmatrix} {}^ib_i(x) \\ {}^ib_i(y) \\ {}^ib_i(z) \end{pmatrix} = \frac{\mu_0 N a^2}{2(a^2 + {}^iz^2)^{\frac{3}{2}}} \begin{pmatrix} 0 \\ 0 \\ I_i \end{pmatrix}, \tag{1} $$

where $\vec{I} = (I_1,\, I_2,\, I_3,\, I_4)^T$ is the current vector consisting of traversing current of coil i, I_i, μ_0 ($= 4\pi \cdot 10^{-7}$ H/m) is the vacuum permeability, a ($= 21$ cm) is the diameter of coil, and N ($= 125$ turns) is the number of turns of wire of each coil. Due to the symmetry, $\vec{b}_x = \vec{b}_y = 0$.

The rotation matrix R_i for coil i to coincide the directions of axes of local frames ${}^i\hat{x}\hat{y}\hat{z}$ with those of global frame ${}^G\hat{X}\hat{Y}\hat{Z}$ can be expressed with Euler angles as

$$ R_i = R({}^i\hat{x}, -\frac{\pi}{4}) R({}^i\hat{z}', \phi_i), \tag{2} $$

where

$$R({}^{i}\hat{x},\theta) = \begin{bmatrix} 1 & 0 & 0 \\ 0 & \cos\theta & -\sin\theta \\ 0 & \sin\theta & \cos\theta \end{bmatrix} \tag{3}$$

and

$$R({}^{i}\hat{z}',\phi) = \begin{bmatrix} \cos\phi & -\sin\phi & 0 \\ \sin\phi & \cos\phi & 0 \\ 0 & 0 & 1 \end{bmatrix}. \tag{4}$$

Here $\phi_i = -\frac{\pi}{4}, -\frac{3\pi}{4}, \frac{3\pi}{4}$, and $\frac{\pi}{4}$ for coils $i = 1, ..., 4$, respectively, and ${}^{i}\hat{z}'$ is newly created axis by the first rotation about $\hat{x}$.

${}^{i}\vec{b}_i$ in the global coordinate ${}^{G}\vec{b}_i$ can be therefore obtained as

$${}^{G}\vec{b}_i = R^{-1}({}^{i}\hat{z}',\phi)\, R^{-1}({}^{i}\hat{x}, -\frac{\pi}{4})\, {}^{i}\vec{b}_i. \tag{5}$$

The globally created magnetic flux density by four coils ${}^{G}\vec{B}$ is given by the superposition of the individual magnetic flux densities ${}^{G}\vec{b}_i$ produced by respective coils, represented in the global coordinate, ${}^{G}\vec{b}_i$, as

$$\begin{aligned} {}^{G}\vec{B} &= \sum_{i=1}^{4} {}^{G}\vec{b}_i && (6)\\ &= \sum_{i=1}^{4} R^{-1}({}^{i}\hat{z}',\phi)\, R^{-1}({}^{i}\hat{x}, -\frac{\pi}{4})\, {}^{i}\vec{b}_i && (7)\\ &:= J(\hat{X},\hat{Y},\hat{Z})\, \vec{I}, && (8) \end{aligned}$$

where

$$J(\hat{X},\hat{Y},\hat{Z}) = \frac{\mu_0 N a^2}{2(a^2 + \frac{d^2}{4})^{\frac{3}{2}}} \begin{bmatrix} \frac{1}{2} & \frac{1}{2} & -\frac{1}{2} & -\frac{1}{2} \\ -\frac{1}{2} & \frac{1}{2} & \frac{1}{2} & -\frac{1}{2} \\ \frac{1}{\sqrt{2}} & \frac{1}{\sqrt{2}} & \frac{1}{\sqrt{2}} & \frac{1}{\sqrt{2}} \end{bmatrix}, \tag{9}$$

relating current $\vec{I}$ to magnetic flux density ${}^{G}\vec{B}$. (9) shows that (6) is linear in the current $\vec{I}$.

As J is full-rank, ${}^{G}\vec{B}$ produced at the center of the stage can be along any spherical direction and be of arbitrary strength up to the system's capacity. Our model can produce maximum magnetic flux density of $1.75\,\mathrm{mT}$ with current $48\,\mathrm{A}$, though this value can be varied by regulating the current flow or the number of wire turns in each coil.

One solution for the current $\vec{I}$ required to generate a desired magnetic flux density ${}^{G}\vec{B}$ at the stage can be determined by solving the unconstrained least squares problem

$$\underset{\vec{I}}{\text{minimize}} \; \| J(\hat{X}, \hat{Y}, \hat{Z})\, \vec{I} - {}^{G}\vec{B}(\hat{X}, \hat{Y}, \hat{Z}) \|_2 \tag{10}$$

corresponding to the undetermined system of (8). The least squares problem (10) can be solved using the Moore-Penrose pseudo inverse of the matrix J

$$\vec{I} = J^{\#}\, {}^{G}\vec{B}, \tag{11}$$

where $J^{\#} = J^T (J J^T)^{-1}$. This minimizes the Euclidean norm of $\vec{I}$, thereby minimizing both energy consumption and heat generation (*39*).

We obtain

$$J^{\#} = \frac{2(a^2 + \frac{d^2}{4})^{\frac{3}{2}}}{\mu_0 N a^2} \begin{bmatrix} \frac{1}{2} & -\frac{1}{2} & \frac{1}{2\sqrt{2}} \\ \frac{1}{2} & \frac{1}{2} & \frac{1}{2\sqrt{2}} \\ -\frac{1}{2} & \frac{1}{2} & \frac{1}{2\sqrt{2}} \\ -\frac{1}{2} & -\frac{1}{2} & \frac{1}{2\sqrt{2}} \end{bmatrix}. \tag{12}$$

The attachment mechanisms require precise localization, which can be provided via magnetic sensing, vision, or an external tracking and localization system. While localization using magnetic sensing was demonstrated on our platform in (*44*), due to the complexity of the environment and necessity for multimodal performance, a human operator manually controlled alignment and direction.

In practice, as ${}^{G}\vec{b}_i$ diverges, the system experiences deviations in the direction and strength of ${}^{G}\vec{B}$ at around the edge of the workspace. To warrant the controllability of robots, the system was designed with four coils instead of the minimum number, three, to reasonably cancel out the deviations of the field strengths by oppositely positioning coils (close one and distant one). Additionally, the diameter of the coils was set such that their normal projections onto the stage cover the entire area and minimizes the deviation in the direction of produced magnetic field.

Primer **Control**

Primer has an edge length of $3.18\,\mathrm{mm}$, weighs $0.24\,\mathrm{g}$, with a surface field of $0.65\,\mathrm{T}$ (***K&J magnetics***). By regarding the magnet as a magnetic dipole $\vec{m} := (m(X),\, m(Y),\, m(Z))^T$, the magnetic torque $\vec{\tau}$ acting on the magnet due to ${}^G\vec{B}$ is given by

$$\vec{\tau} = \vec{m} \times {}^G\vec{B} \tag{13}$$

$$= \begin{bmatrix} 0 & -m(Z) & m(Y) \\ m(Z) & 0 & -m(X) \\ -m(Y) & m(X) & 0 \end{bmatrix} {}^G\vec{B}. \tag{14}$$

We experimentally estimated $m = 0.030\,\mathrm{Am}^2$ by measuring required torque to rotate *Primer*. With (8) and (14) follows that $\vec{\tau}$ is linear in the currents $\vec{I}$. Therefore,

$$\vec{\tau} := J_\tau\, \vec{I}, \tag{15}$$

where

$$J_\tau = \frac{\mu_0 N a^2}{2(a^2 + \frac{d^2}{4})^{\frac{3}{2}}} \cdot \begin{bmatrix} -\frac{1}{2}m(Z) - \frac{1}{\sqrt{2}}m(Y) & \frac{1}{2}m(Z) - \frac{1}{\sqrt{2}}m(Y) \\ \frac{1}{2}m(Z) - \frac{1}{\sqrt{2}}m(Y) & -\frac{1}{2}m(Z) - \frac{1}{\sqrt{2}}m(Y) \\ -\frac{1}{2}m(Z) + \frac{1}{\sqrt{2}}m(X) & -\frac{1}{2}m(Z) + \frac{1}{\sqrt{2}}m(X) \\ \frac{1}{2}m(Z) + \frac{1}{\sqrt{2}}m(X) & \frac{1}{2}m(Z) + \frac{1}{\sqrt{2}}m(X) \\ \frac{1}{2}m(Y) + \frac{1}{2}m(X) & \frac{1}{2}m(Y) - \frac{1}{2}m(X) \\ -\frac{1}{2}m(Y) - \frac{1}{2}m(X) & -\frac{1}{2}m(Y) + \frac{1}{2}m(X) \end{bmatrix} \tag{16}$$

which relates current $\vec{I}$ to torque $\vec{\tau}$. We estimate $\tau_{\max} = 5.25 \cdot 10^{-5}\,\mathrm{Nm}$ ($0.535\,\mathrm{g\text{-}f\,cm}$) under the application of ${}^G B = 1.75\,\mathrm{mT}$, which assures the possible-to-lift surface area of $1.21\,\mathrm{cm}^2$ assuming that the sheet is flat square, the density of second exoskeleton sheet $0.0344\,\mathrm{g/cm}^2$, and the magnet positions at the center of the sheet. Based on the calculation, the developed exoskeletons have off-centered *Primer* positions close to the pivoting point to reduce the required torque, with comprehensive body structures to enable larger exoskeleton sizes.

Walk-bot

The *Walk-bot* design is shown in Fig. S2. The unfolded exoskeleton has size $23.72 \times 8.09\,\mathrm{mm}^2$. When folding, the creases consisting of 13 mountain folds and 17 valley folds self-fold, encasing

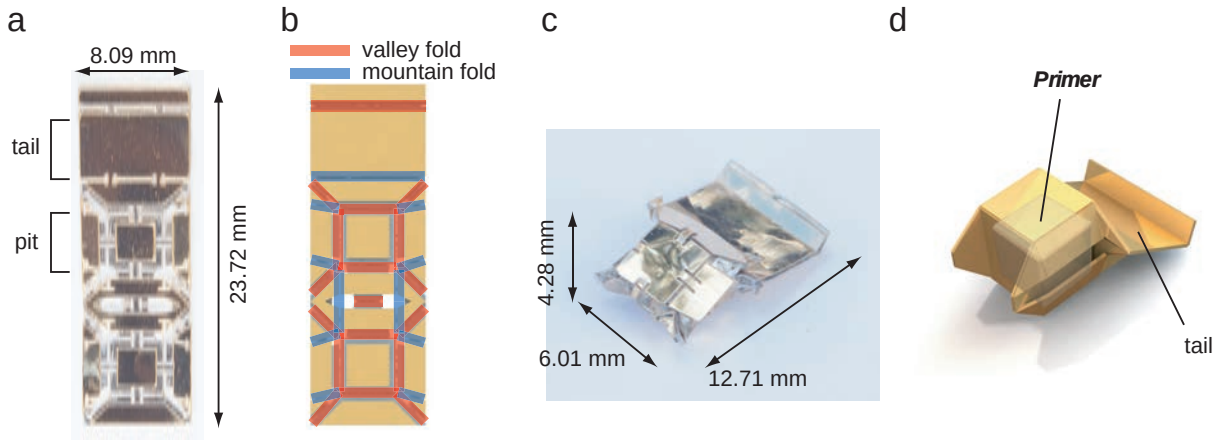

Figure S2: *Walk-bot* design. (a,b) unfolded configurations, and (c,d) folded configurations.

Primer completely. The average time taken for self-folding of *Walk-bot* is $173\,\mathrm{s}$ (5 samples). The speed typically depends on the capacity of the Peltier element and can be increased by using another type or soaking in hot water (*46*). Once self-folded, *Walk-bot* stands at $4.25\,\mathrm{mm}$ tall and is $10.43 \times 7.81\,\mathrm{mm}^2$. It weighs $0.289\,\mathrm{g}$ while merely 17% of the weight is from the exoskeleton (the rest is from *Primer*). The walking motion is based on stick-slip motion presented also in (*29*).

Scaled walk-bot

The design of *Scaled walk-bot* is shown in Fig. S3. It weighs $0.539\,\mathrm{g}$; *Walk-bot* including *Primer* weighs $0.289\,\mathrm{g}$, which is 53.6% of the total weight. The basic crease pattern was inherited from *Walk-bot* but without the front segment that reconfigures to a ceiling. Instead, four arms are provided at the location of *Walk-bot*, facing the short edge. A self-folding process turns the unfolded sheet of $32.82 \times 22.14\,\mathrm{mm}^2$ into *Scaled walk-bot* ($26.9 \times 21.94 \times 6.11\,\mathrm{mm}^3$). The

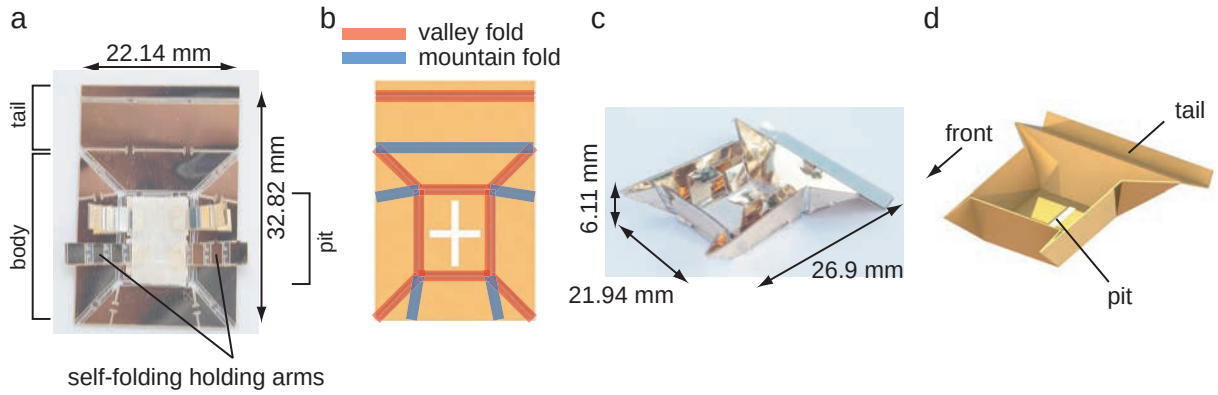

Figure S3: *Scaled walk-bot* design. (a,b) unfolded configurations, and (c,d) folded configurations.

process involves 5 mountain folds and 9 valley folds. The average self-folding speed of a second exoskeleton is 158 s (5 samples). The body size was chosen according to the maximum amount of magnetic torque we can impose. The tail was shortened to reduce the amount of torque required to pivot.

The *Scaled walk-bot* is particularly useful as a miniature shovel. To demonstrate its effectiveness, we measured the carriable number of $\sim$ 5 mm polyethylene foam blocks of 2 mg for *Scaled walk-bot* and *Walk-bot*. While *Walk-bot* was able to carry at most one block at a time, *Scaled walk-bot* could carry between 3 and 5 blocks at one time.

The experiment of 2-step metamorphoses and molting processes shown in Fig. 2 (a)-(f) was iterated for 5 times and we obtained 2 end-to-end successes. The time taken for the whole process was around 20 min in average (3 samples). The variable time was spent aligning *Walk-bot* to the exoskeleton and waiting for the latches to dissolve. The main reason for the failure is misalignment of *Walk-bot* in the exoskeleton of *Scaled walk-bot*. While *Walk-bot* can walk under water, the capillary force prevents it from coming ashore. In experiments, we employed rolling motion for *Walk-bot* when it climbed the slope. The success and failure of events occurring in each trial are detailed in Table 1.

Table 1: Success and failure events with *Scaled walk-bot*.

	Primer alignment	*Walk-bot* self-folding	*Walk-bot* walking	*Walk-bot* alignment	*Scaled walk-bot* self-folding	*Scaled walk-bot* walking	*Scaled walk-bot* dissolving	*Walk-bot* molting
Trial 1	Yes	Yes	Yes	No	No	No	No	No
Trial 2	Yes	Yes	Yes	Yes	Yes	No	Yes	Yes
Trial 3	Yes	Yes	No	No	No	No	No	No
Trial 4	Yes	Yes	Yes	Yes	Yes	Yes	Yes	Yes
Trial 5	Yes	Yes	Yes	Yess	Yes	Yes	Yes	Yes

Wheel-bot

The design of *Wheel-bot* is shown in Fig. S4. The unfolded exoskeleton of *Wheel-bot* has a

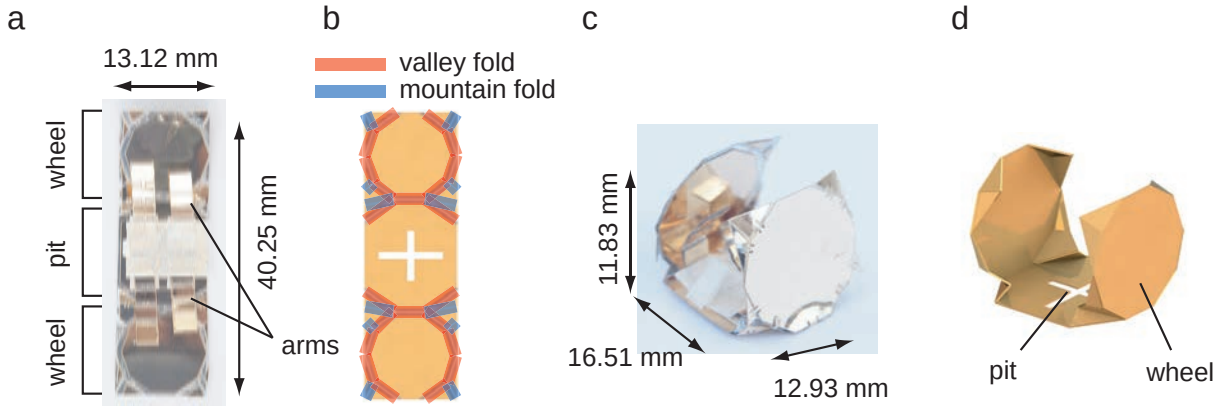

Figure S4: *Wheel-bot* design. (a,b) unfolded configurations, and (c,d) folded configurations.

dimension of $40.25 \times 13.12\,\mathrm{mm}^2$ and consists of three blocks. It weighs $0.43\,\mathrm{g}$, while *Walk-bot* including *Primer* weighs $0.298\,\mathrm{g}$. *Walk-bot* sits at the pit facing the longitudinal edge. When heated, 12 mountain and 20 valley folds self-fold, and two parts on both ends transform into decagonal wheels perpendicularly folding up. The angle of the wheel is regulated with a pair of mountain and valley folds, and the angle converges near perpendicularly to the pit. It achieves a dimension of $12.93 \times 16.51 \times 11.83\,\mathrm{mm}^3$. Ideally, the *Primer* should be positioned around the wheel axis. However, such design would require elevation of *Walk-bot* while self-folding, and *Walk-bot* could fall out of the latch. Once reconfiguration is completed, a rotational magnetic field of $1.75\,\mathrm{mT}$ is applied for rolling motion. In experiments, the frequency is set at $0.73\,\mathrm{Hz}$.

Fig. S5 shows the rolling speed of *Wheel-bot* over the frequency of rotational magnetic field. As expected, the speed linearly increases proportional to the frequency until step-out

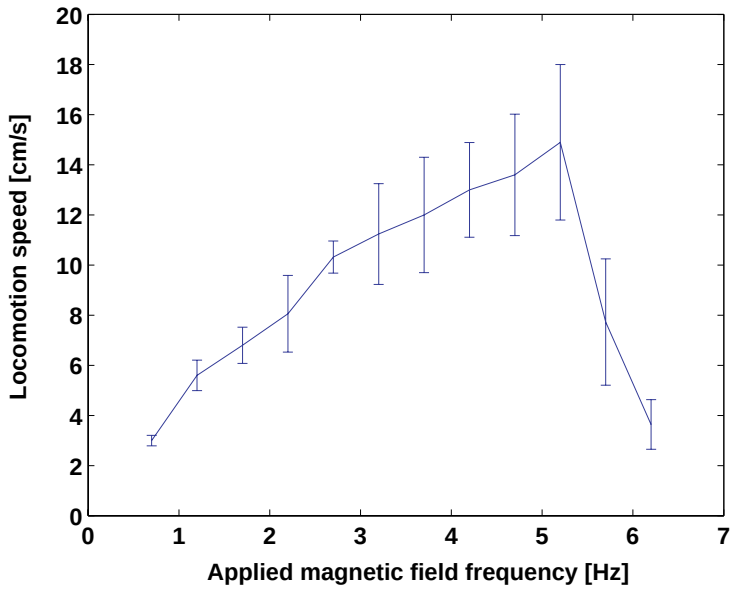

Figure S5: The rolling speed of *Wheel-bot* over frequency of magnetic field applied (5 samples).

occurs after 5 Hz. *Wheel-bot* rolls at a maximum speed of 14.8 cm/s, while *Walk-bot* walks at a maximum speed of 5.84 cm/s, showing the efficiency of rolling on ground (270% faster).

The robot capability enabled by the wheel exoskeleton added to *Walk-bot* is shown in Fig. S6. Due to the simple crease pattern, the entire process shows reliable performance. The trial was repeated 5 times with 4 successes. The success and failure of events occurring in each trial are detailed in Table 2.

Boat-bot

Boat-bot shows stability when controlled on water and can move on ground using stick-slip motion due to the forward placement of the magnet. Fig. S7 shows the crease pattern (a,b) and the self-folded *Boat-bot* (c,d). The unfolded exoskeleton sheet ($31.44 \times 19.64\,\text{mm}^2$, 0.496 g)

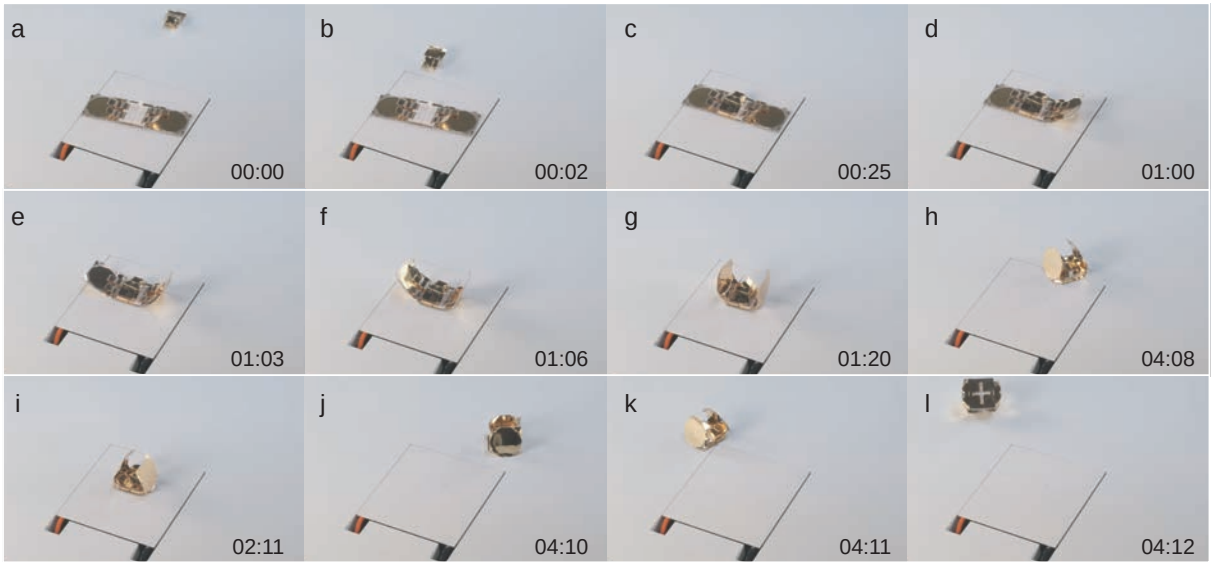

Figure S6: Demonstration of *Wheel-bot*. (a-c) *Walk-bot* approaches and steps on the wheel exoskeleton. (d-i) The exoskeleton starts heat-triggered self-folding, (j-l) forms two wheels on both sides, and starts rolling, guided by a magnetic field. The entire experiment is presented in Movie 2.

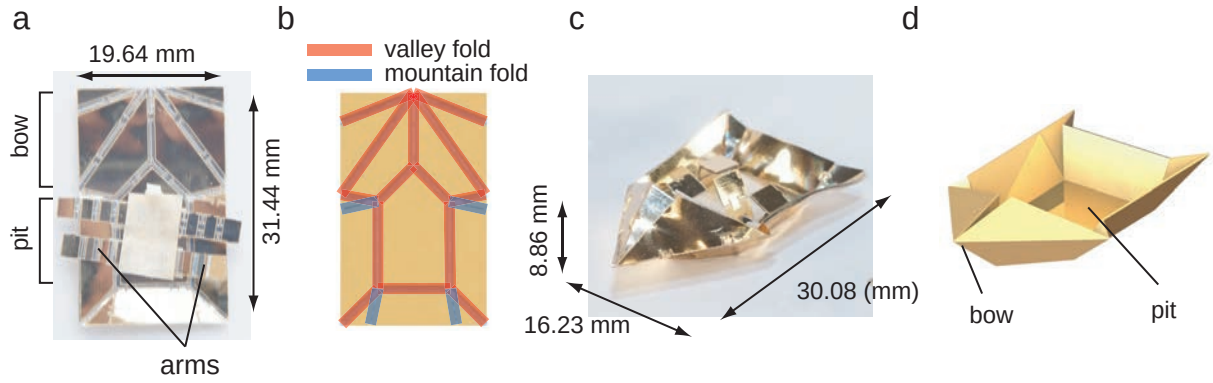

Figure S7: *Boat-bot* design. (a,b) unfolded configurations, and (c,d) folded configurations.

self-folds into a boat shape of $30.08 \times 16.23 \times 8.86\,\text{mm}^3$ by lifting the sides up, forming a concave shape around the pit. The process involves 4 mountain and 14 valley folds, which self-fold into a concave body shape for floating.

For actuation on water, we employ magnetic force induction with field gradient. Given no

Table 2: Success and failure events with *Wheel-bot*.

	Walk-bot alignment	*Wheel-bot* self-folding	*Wheel-bot* rolling	*Wheel-bot* dissolving	*Walk-bot* molting
Trial 1	Yes	Yes	Yes	Yes	Yes
Trial 2	Yes	Yes	Yes	Yes	Yes
Trial 3	Yes	Yes	Yes	Yes	Yes
Trial 4	Yes	Yes	Yes	Yes	Yes
Trial 5	Yes	Yes	No	Yes	Yes

current is running in the space occupied by *Primer*, the magnetic force F acting on *Primer* with magnetic moment $\vec{m}$ due to ${}^{G}\vec{B}$ is given by

$$\vec{F} = (\vec{m} \cdot \nabla)\, {}^{G}\vec{B} \tag{17}$$

$$= \begin{bmatrix} \frac{\partial\, {}^{G}\vec{B}(X)}{\partial X} & \frac{\partial\, {}^{G}\vec{B}(X)}{\partial Y} & \frac{\partial\, {}^{G}\vec{B}(X)}{\partial Z} \\ \frac{\partial\, {}^{G}\vec{B}(Y)}{\partial X} & \frac{\partial\, {}^{G}\vec{B}(Y)}{\partial Y} & \frac{\partial\, {}^{G}\vec{B}(Y)}{\partial Z} \\ \frac{\partial\, {}^{G}\vec{B}(Z)}{\partial X} & \frac{\partial\, {}^{G}\vec{B}(Z)}{\partial Y} & \frac{\partial\, {}^{G}\vec{B}(Z)}{\partial Z} \end{bmatrix} \begin{pmatrix} m(X) \\ m(Y) \\ m(Z) \end{pmatrix} \tag{18}$$

$$= \begin{pmatrix} \frac{\partial\, {}^{G}\vec{B}}{\partial X} m(X) \\ \frac{\partial\, {}^{G}\vec{B}}{\partial Y} m(Y) \\ \frac{\partial\, {}^{G}\vec{B}}{\partial Z} m(Z) \end{pmatrix}. \tag{19}$$

From (7), we obtain

$$\frac{\partial\, {}^{G}\vec{B}}{\partial X} = \sum_{i=1}^{4} \frac{\partial}{\partial X} \vec{b}_i \tag{20}$$

$$= \sum_{i=1}^{4} \frac{\partial}{\partial z_i} \frac{\partial z_i}{\partial X} \frac{\mu_0 N a^2 I_i}{2(a^2 + z_i^2)^{\frac{3}{2}}} \tag{21}$$

$$= \frac{3\mu_0 N a^2}{4} \left\{ -\sum_{i=1}^{2} \left(\frac{z_i^2 I_i}{(a^2 + z_i^2)^{\frac{5}{2}}} \right) + \sum_{i=3}^{4} \left(\frac{z_i^2 I_i}{(a^2 + z_i^2)^{\frac{5}{2}}} \right) \right\}. \tag{22}$$

By substituting $z_i = \frac{d}{2}$ for all i, we obtain

$$\frac{\partial\, {}^{G}B}{\partial X} = \frac{3}{4} \mu_0 N a^2 \left\{ \frac{\frac{d^2}{4}}{(a^2 + \frac{d^2}{4})^{\frac{5}{2}}} \right\} (-I_1 - I_2 + I_3 + I_4). \tag{23}$$

Similarly, we obtain

$$\frac{\partial\, {}^{G}B}{\partial Y} = \frac{3}{4} \mu_0 N a^2 \left\{ \frac{\frac{d^2}{4}}{(a^2 + \frac{d^2}{4})^{\frac{5}{2}}} \right\} (I_1 - I_2 - I_3 + I_4) \tag{24}$$

and

$$\frac{\partial\, {}^{G}B}{\partial Z} = \frac{3}{2\sqrt{2}}\mu_0 N a^2 \left\{ \frac{\frac{d^2}{4}}{(a^2+\frac{d^2}{4})^{\frac{5}{2}}} \right\} (-I_1 - I_2 - I_3 - I_4). \tag{25}$$

(17)-(25) suggest that $\vec{F}$ is linear in the current $\vec{I}$ and can be rewritten as

$$\vec{F} = J_F\, \vec{I}, \tag{26}$$

where

$$\begin{aligned} J_F =& \frac{3}{4}\mu_0 N a^2 \left\{ \frac{\frac{d^2}{4}}{(a^2+\frac{d^2}{4})^{\frac{5}{2}}} \right\} \cdot \\ & \begin{bmatrix} -m(X) & -m(X) & m(X) & m(X) \\ m(Y) & -m(Y) & -m(Y) & m(Y) \\ -\sqrt{2}m(Z) & -\sqrt{2}m(Z) & -\sqrt{2}m(Z) & -\sqrt{2}m(Z) \end{bmatrix}, \end{aligned} \tag{27}$$

which relates current $\vec{I}$ to force $\vec{F}$.

We use negative currents $I_i \leq 0$ and always use attractive force for swimming control regardless of the position of the *Primer* on the stage. With (23), we estimate magnetic force $F(X) = 0.0378\,\text{mN}$ under application of $I_1 = I_2 = -10\,\text{A}$ assuming that a magnet is pointing toward the positive direction of $\hat{X}$-axis.

With (15) and (26) follows

$$\begin{pmatrix} \vec{\tau} \\ \vec{F} \end{pmatrix} = \begin{bmatrix} J_\tau \\ J_F \end{bmatrix} \vec{I} := A\, \vec{I}, \tag{28}$$

where A is a 6×4 actuation matrix describing the torque and force acting on a magnet inside the area of operation due to the currents applied by the four electromagnetic coils. By solving the inverse of A, we obtain required $\vec{I}$ for desired $\vec{F}$ and $\vec{\tau}$. This linear transformation enables real-time production of magnetic field in response to the operator's control input.

The payload of *Boat-bot* was measured by placing increasing weight ($\varnothing 2.38\,\text{mm}$, $0.0204\,\text{g}$ aluminum balls) onto the exoskeleton. The result was $0.924 \pm 0.066\text{g}$ (5 samples) before it

sank. Given the weight of *Walk-bot* is 0.496 g, it carries 1.86 times its weight by equipping the boat exoskeleton.

The entire experiment with *Boat-bot*, starting with *Walk-bot* is shown in Fig. S8. The process

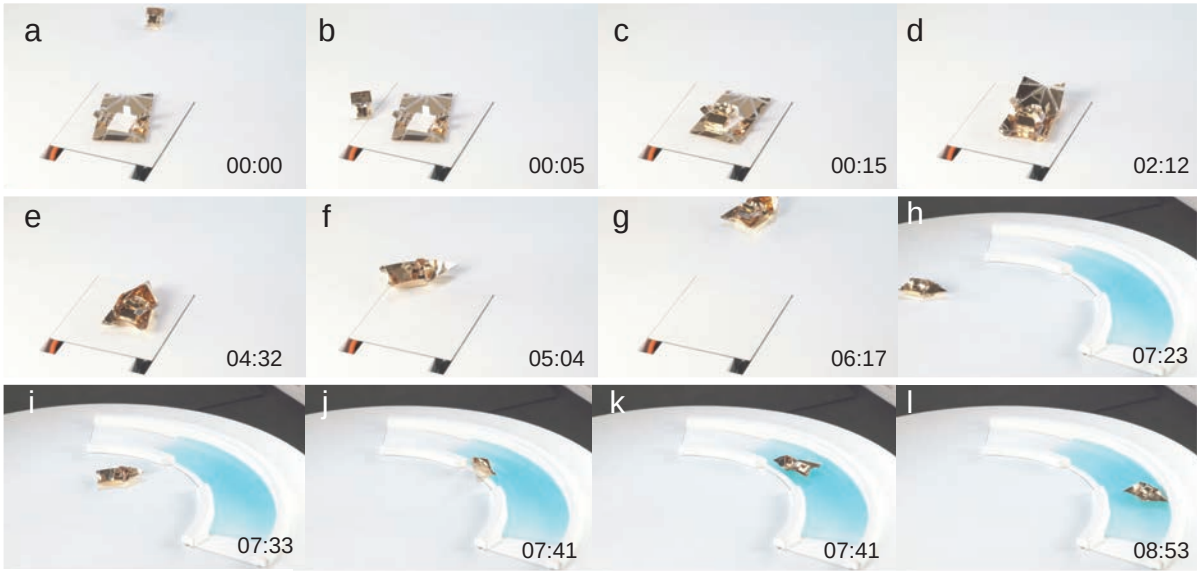

Figure S8: Demonstration with boat exoskeleton. The *Walk-bot* walks in and rides on the pit of the boat exoskeleton (a-c). The exoskeleton starts self-folding (d), and completes reconfiguration (e). The folded exoskeleton walks and enters the reservoir (f-i). It shows swimming capability on water (j-l). The entire experiment is presented in Movie 3.

was iterated 5 times and 3 successful results were obtained. We detailed the success and failure of events occurring in each trial in Table 3. In the two failure trials, *Boat-bot* failed to walk due to misalignment of *Walk-bot*.

Glider-bot

The exoskeleton of *Glider-bot* and the folded configurations are shown in Fig. S9. The design requires extensive considerations of weight and strength for the structure, and aerodynamics for the gliding motion. Additionally, there are design constraints from the size of Peltier element,

Table 3: Success and failure events with *Boat-bot*.

	Walk-bot alignment	*Boat-bot* self-folding	*Boat-bot* walking	*Boat-bot* floating
Trial 1	Yes	Yes	No	Yes
Trial 2	Yes	Yes	No	No
Trial 3	Yes	Yes	Yes	Yes
Trial 4	Yes	Yes	Yes	Yes
Trial 5	Yes	Yes	Yes	Yes

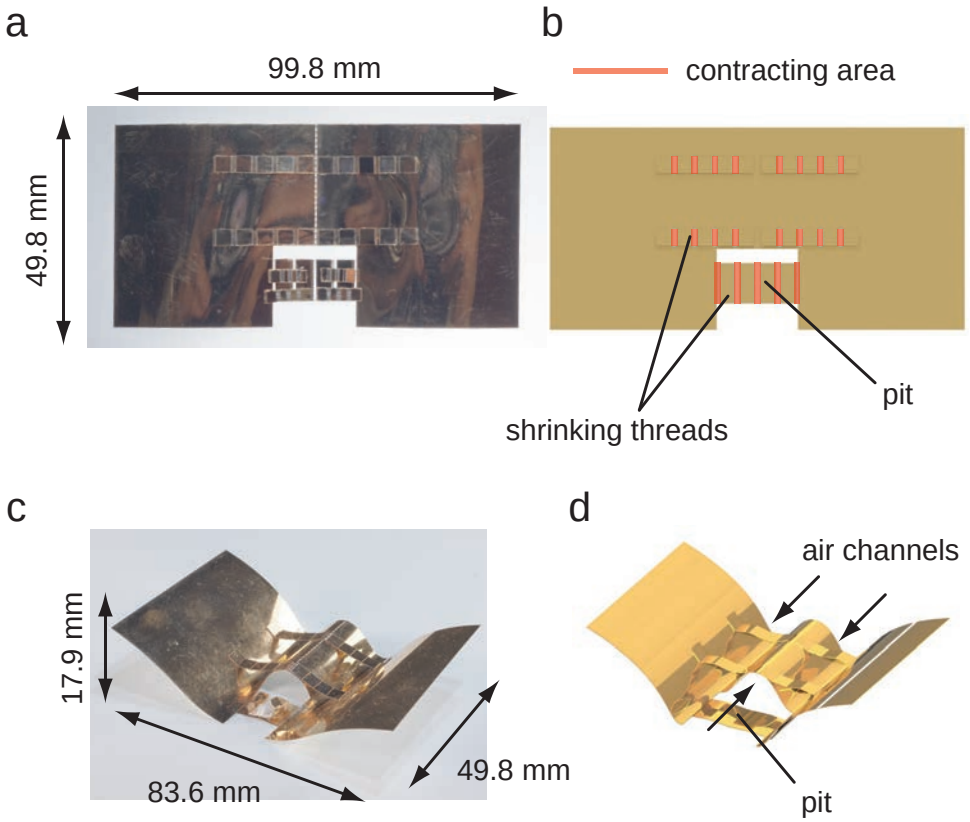

Figure S9: *Glider-bot* design. (a,b) unfolded configurations and (c,d) folded configurations.

that all the contracting threads should fit in the area. In order to increase the stability about the roll axis, the *Glider-bot* has a W-shaped body with three cylindrical opening channels. This design allows the wing on each side to be kept upward with a dihedral angle of approximately $33 \pm 2^{\circ}$ (6 samples). Moreover, these symmetrical channels act as stabilizers to keep the robot's

gliding posture without yaw motion. To form the wing shape, six linear heat-sensitive shrinking threads are attached. When heat is applied to the structure, the threads contract and produce the curved wing shape. This design lowers the center of mass and lifts up the wing, enabling a proper gliding posture with stability about the pitch axis. The structure can be made with a single layer and thus it is lightweight while maintaining enough rigidity against twisting and bending when gliding. In addition, the shape provides a space for the pit for *Walk-bot* to position itself. The sheet has a dimension $99.8 \times 49.8\,\text{mm}^2$ and once it configures as *Glider-bot* it has a dimension $83.6 \times 49.8 \times 17.9\,\text{mm}^3$. The body of *Glider-bot* exoskeleton weighs $0.585\,\text{g}$ and the body of *Glider-bot* including *Walk-bot* weighs $0.825\,\text{g}$.

We have demonstrated a successful end-to-end cycle for gliding. The success and failure of events occurring in each trial are detailed in Table 4. The main reasons for failure were

Table 4: Success and failure events with *Glider-bot*.

	Walk-bot alignment	*Glider-bot* self-folding	*Glider-bot* ramp sliding	*Glider-bot* gliding
Trial 1	Yes	Yes	Yes	Yes
Trial 2	Yes	Yes	No	No
Trial 3	Yes	Yes	Yes	No
Trial 4	Yes	Yes	Yes	No
Trial 5	Yes	No	No	No

misalignment of the walk bot on exoskeleton, misfolding of the *Glider-bot* exoskeleton (the wings would buckle or fold non-symetrically), and inability to fly once folded. The challenge has been alignment with the gliding ramp, due to the significantly larger size of *Glider-bot*. Producing a glider at this scale with self-folding methods has proven to be an exacting process where even a small misalignment of Walk-bot could spell the difference between success and failure. Our challenge was designing around the immense difficulties of flight at this scale, to which we have achieved a complete successful end-to-end cycle.

Multimedia Extension

We provide four movies that display the typical metamorphic behavior of (1) *Scaled walk-bot* as shown in Fig. 2 (Movie 1), (2) *Wheel-bot* as shown in Fig. S6 (Movie 2), (3) *Boat-bot* as shown in Fig. S8 (Movie 3), and (4) *Glider-bot* as shown in Fig. 2 (Movie 4).